Energy Advances

ROYAL SOCIETY OF CHEMISTRY

PAPER

View Article Online
View Journal | View Issue

Cite this: *Energy Adv.*, 2023, 2, 1419

Construction of $Co_3(PO_4)_2$/g-C_3N_4 nanowire composites to boost visible-light-driven photocatalysis

Haiqin Jiang, Jinlun Li, Xi Rao * and Yongping Zhang *

Received 4th June 2023,
Accepted 22nd July 2023

DOI: 10.1039/d3ya00253e

rsc.li/energy-advances

$Co_3(PO_4)_2$/g-C_3N_4 nanowire composites are prepared by calcining a certain amount of melamine and cobalt phosphate (CPO) nanowires at 550 °C in a nitrogen environment, forming a heterojunction structure of $Co_3(PO_4)_2$ nanowires with a size of 10–20 nm embedded in g-C_3N_4 (CN) sheets. The introduction of $Co_3(PO_4)_2$ nanowires broadens the visible light absorption range of g-C_3N_4, increases the specific surface area, and greatly enhances the transfer and separation of photogenerated charge carriers. Under visible light irradiation, the hydrogen evolution rate of the 15CPO–CN photocatalyst (10 mg) reached an optimal value of up to 29.31 μmol h^{-1}, about 10 times that of pure CN (2.89 μmol h^{-1}) and it showed enhanced antibacterial activity for removing *E. coli* as well. The synergic effect of the heterojunction between CPO nanowires and CN sheets accelerates the charge separation and transfer from CN to CPO, thus improving the photocatalytic activity.

1. Introduction

Photocatalysts were widely used in solving environmental pollution and energy shortage problems, such as photocatalytic pollutant degradation, antibacterial activity and hydrogen production.[1–4] As a new and promising photocatalyst, graphitic carbon nitride (g-C_3N_4) has attracted extensive interest because of its visible light response, excellent chemical stability and easy preparation technique. Meanwhile, its appropriate electronic band structure meets the prerequisites for hydrogen evolution and oxygen evolution in the water splitting process. Some shortcomings limited its further application, such as the rapid recombination of photogenerated electron/hole pairs and the low visible light response. Various strategies were carried out to improve the photocatalytic activity, including element doping, nanostructure formation, and heterojunction construction.[5–12] Designing g-C_3N_4 heterojunction composites by hybridizing other semiconductors with appropriate conduction band and valence band potentials remains a promising method to further improve the photocatalytic activity.

Cobalt phosphate ($Co_3(PO_4)_2$) is a promising candidate because of its economy, narrow band gap, strong visible light capture ability, non-toxicity and environmental compatibility.[13,14] More importantly, $Co_3(PO_4)_2$ not only has an energy band position suitable for overall water splitting, but also has a matching energy level with g-C_3N_4, which makes it possible to design $Co_3(PO_4)_2$/g-C_3N_4 nanocomposites to achieve water splitting. Recently, $Co_3(PO_4)_2$/g-C_3N_4 heterostructure photocatalysts with 0D, 2D and 3D morphologies have been synthesized using a photo-deposition method, demonstrating enhanced photocatalytic activity.[15–19] However, the roles of $Co_3(PO_4)_2$ in the heterojunction and band structure were not well understood. The enhanced photocatalytic activity was credited to type II, Z heterojunctions or carrier transfer relay. Even the band gap of $Co_3(PO_4)_2$ was measured to be different values in different references, such as 2.32 eV in ref. 15 and 1.93 eV in ref. 19. Further investigation is needed to provide detailed information to understand its mechanism. On the other hand, 1D nanowires were found to exhibit great specific surface areas and favor electron transfer, and 1D nanowire $Co_3(PO_4)_2$ composites have not been reported so far.[9,20] We proposed a pathway to construct $Co_3(PO_4)_2$/g-C_3N_4 nanowire composites. Firstly, $Co_3(PO_4)_2$ nanowires were synthesized using a hydrothermal method, then mixed with melamine, and calcined in a tubular furnace. Finally $Co_3(PO_4)_2$/g-C_3N_4 nanocomposite photocatalysts were successfully prepared with excellent photocatalytic performance.

Herein, $Co_3(PO_4)_2$/g-C_3N_4 nanocomposite photocatalysts were prepared by calcining the mixture of $Co_3(PO_4)_2$ nanowires and melamine. Introducing $Co_3(PO_4)_2$ nanowires into g-C_3N_4 sheets extended the visible light harvesting, increased the specific surface area, and facilitated the separation and transfer of photoinduced electron/hole pairs, resulting in $Co_3(PO_4)_2$/g-C_3N_4 composites with excellent photocatalytic performance.

School of Materials and Energy, Southwest University, Chongqing 400715, China.
E-mail: raoxiemail@swu.edu.cn, zhangyyping6@swu.edu.cn

2. Experimental details

2.1. Chemicals

All chemicals (AR grade), including melamine (99%), $Co(NO_3)_2{\cdot}6H_2O$ (99%), and $(NH_4)_2HPO_4$ (98%), were purchased from Sinopharm Chemical Reagent Co. Ltd and were used without further purification.

2.2. Catalyst preparation

$Co_3(PO_4)_2$ nanowires: 0.165 g $Co(NO_3)_2{\cdot}6H_2O$ was fully dissolved in 50 mL deionized water by constant ultrasonic stirring, marked as solution A. 0.05 g $(NH_4)_2HPO_4$ was dissolved in 30 mL deionized water as solution B. Then, solution B was injected into solution A dropwise using a microsyringe at room temperature under ultrasonic stirring, and transferred into a stainless steel autoclave, kept at 200 °C for 20 h. The precipitate was centrifuged, washed and dried to collect $Co_3(PO_4)_2$ nanowires, denoted as CPO.

$Co_3(PO_4)_2$/g-C_3N_4 composite: 2.0 g melamine and a certain amount of CPO (5 wt%, 10 wt%, 15 wt%, and 20 wt% in the ratio of CPO/melamine) were dissolved in 50 mL deionized water under constant stirring, then dried at 75 °C overnight to obtain the mixture powder. The powder was calcined at 550 °C for 4 h at a rate of 5 °C min^{-1} under a N_2 atmosphere to obtain $Co_3(PO_4)_2$/g-C_3N_4 composites, denoted as CPO-CN. Pure g-C_3N_4 was obtained by calcining 5 g melamine at 550 °C for 4 h at a rate of of 5 °C min^{-1} under a N_2 atmosphere, denoted as CN.

2.2. Characterization

Catalysts were characterized using a scanning electron microscope (FESEM, JSM-7800F), transmission electron microscope (TEM, Zeiss Libra 200FE), X-ray diffraction (XRD, Shimadzu XRD7000), Fourier transform infrared spectroscopy (FTIR, Model Frontier), X-ray photoelectron spectroscopy (XPS, VG ESCALAB 250Xi), UV-vis diffuse reflectance spectra (Agilent Cary 5000 UV-vis NIR), photoluminescence (PL, Hitachi F-7000 spectrophotometer), and N_2 adsorption–desorption isotherms (Quadrasorbevo 2QDS-MP-30). The transient photocurrent response curve (*I–t*), Mott–Schottky curve, and electrochemical impedance spectroscopy (EIS) were performed using an AUTOLAB (model PGSTAT302N) electrochemical workstation. A 500 W xenon lamp was used as the light source, and 0.25 M Na_2SO_4 solution as the electrolyte.

2.3. Photocatalytic hydrogen evolution

The photocatalytic hydrogen evolution test was carried out in a photocatalysis evaluation system (Suncat Instrument, Beijing). The 500 W Xe lamp (zolix, gloria-x500a) with an intensity of 110 mW cm^{-2} was used as the simulated solar light with a wavelength $\lambda \geq 420$ nm. The reactor was maintained at 20 °C with an external circulation cooling system. 10 mg photocatalyst was dispersed in 30 mL aqueous solution with 17 vol% triethanolamine (TEOA) as the sacrificing agent and 3 wt% Pt ions ($H_2PtCl_6{\cdot}H_2O$) as the co-catalyst. Before turning on the light, the reactor is pumped to a high vacuum of 10^{-8} torr, and then filled with argon. Under the light irradiation process, the reaction suspension is stirred continuously under magnetic stirring. 1 mL of gas was extracted automatically from the reactor at intervals of 30 min, and analyzed with a gas chromatograph (GC-2018, Shimadzu) with a TDX-01 molecular sieve, thermal conductivity detector and Ar carrier gas.

2.4. Photocatalytic antibacterial activity

The antibacterial activity was determined by co-culture with *Escherichia coli* (*E. coli*) with LB culture medium. 2 mL *E. coli* stock solution and 10 mL LB culture medium were cultured at 37 °C for 16 hours, and diluted with PBS to the bacterial concentration of 10^6 CFU mL^{-1}. CN and 06NSG-CN aqueous solutions with concentrations of 0.1 mg mL^{-1} were prepared and irradiated with ultraviolet light on a sterile ultra clean table for 30 min. Then 1 mL of the above-mentioned solution and 1 mL of 10^6 CFU mL^{-1} *E. coli* solution were mixed in a 24 well plate as the experimental sample; a mixed solution of 1 mL PBS and 1 mL 10^6 CFU mL^{-1} bacterial suspension was used as the blank group. The above-mentioned samples were illuminated for 20 min (500 W xenon lamp, $\lambda > 420$ nm), and then placed in an incubator at 37 °C for 4 h, and diluted with PBS 10^{-2} times. 100 μL of the sample were spread evenly on LB solid medium and cultured at 37 °C for 24 hours. The antibacterial

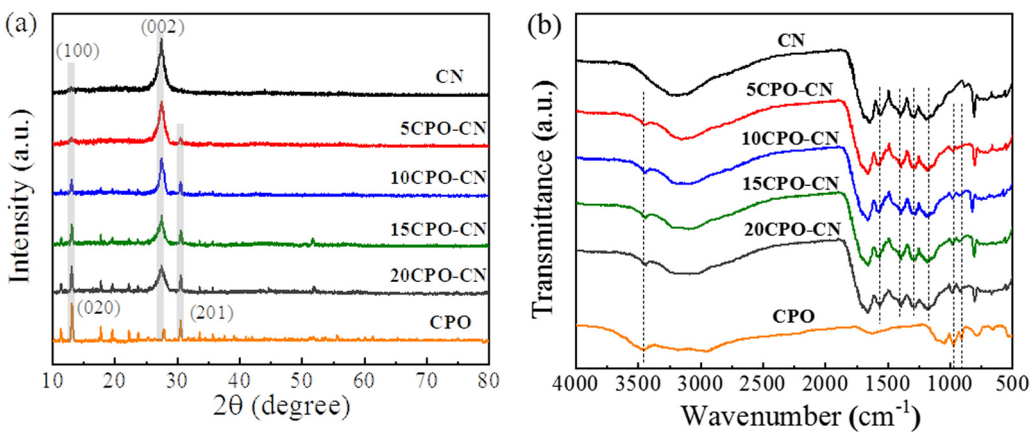

Fig. 1 XRD patterns (a) and FTIR spectra (b) of WO_3/g-C_3N_4 nanocomposites.

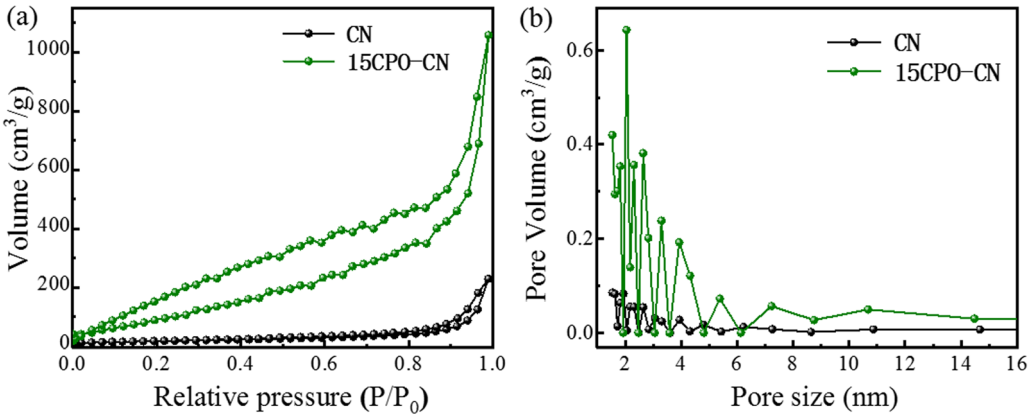

Fig. 2 Nitrogen adsorption–desorption isotherms (a) and pore size distributions (b) of CN and 15CPO–CN nanocomposites.

activity was determined using the plate counting method. For comparison, three groups under the same conditions did not undergo light treatment.

3. Results and discussion

XRD patterns in Fig. 1(a) show the evolution process of CPO–CN with different amounts of CPO added, with CN and CPO as references. There appears to be two characteristic diffraction peaks for the CN sample, the peak at $2\theta = 13.1^\circ$ is ascribed to the (100) crystal plane between 3-*s*-triazine ring repeat unit structures, and the peak at 27.3° to the (002) crystal plane with the layer spacing of the aromatic ring plane structure.[15–17] In the CPO sample, all the diffraction peaks are consistent with the characteristic crystal plane of CPO (JCPDS no. 41-0375).[18] For the CP-CN composites, the two diffraction peaks of g-C_3N_4 remain intact, and all the new characteristic peaks are completely consistent with that of CPO. With the increase of the CPO addition from 5 wt% to 20 wt%, the intensity of the peaks of CPO increases gradually, while that of CN decreases accordingly. In addition, only peaks attributing to g-C_3N_4 and CPO appeared, indicating that the CPO–CN composites are in high purity. The vibration mode of the chemical bond of the sample was determined using a Fourier transform infrared analysis spectrometer. FTIR spectra in Fig. 1(b) show that for CPO, the vibration peak of 663 cm^{-1} corresponds to the stretching vibration of metal–oxygen–metal,[18] peaks near 900–1150 cm^{-1} correspond to the asymmetric stretching vibration of phosphate,[19] while the weak peak concentrated at 1680 cm^{-1}, the wide peaks near 3440 cm^{-1}, and the shoulder near 2900 cm^{-1} correspond to the bending vibration of H–O–H in the interlayer water.[20] In the CN and CP–CN samples, the peak appeared at about 810 cm^{-1}, which is attributed to the characteristic vibration of the tri-*s*-triazine unit in CN. In addition, the peaks in the 1200–1650 cm^{-1} region can be attributed to the stretching vibration of C–N heterocycles in CN. The broad peak near 3250 cm^{-1} is related to the tensile vibration of the N–Hx group at the aromatic ring defect site. Another peak at about 3440 cm^{-1} is attributed to the O–H stretching mode.[21–23] XRD and FTIF results demonstrated that the main characteristic peaks of CN and CPO appeared in the spectra of CP–CN, indicating CPO–CN composites were successfully constructed.

The N_2 adsorption desorption isotherm curves of CN and 15CPO–CN samples are shown in Fig. 2(a). It can be clearly seen that the area of the H3 hysteresis loop of 15CPO–CN increases due to a large number of mesopores on the material surface.[41,42] Fig. 2(b) shows the pore size distribution of the

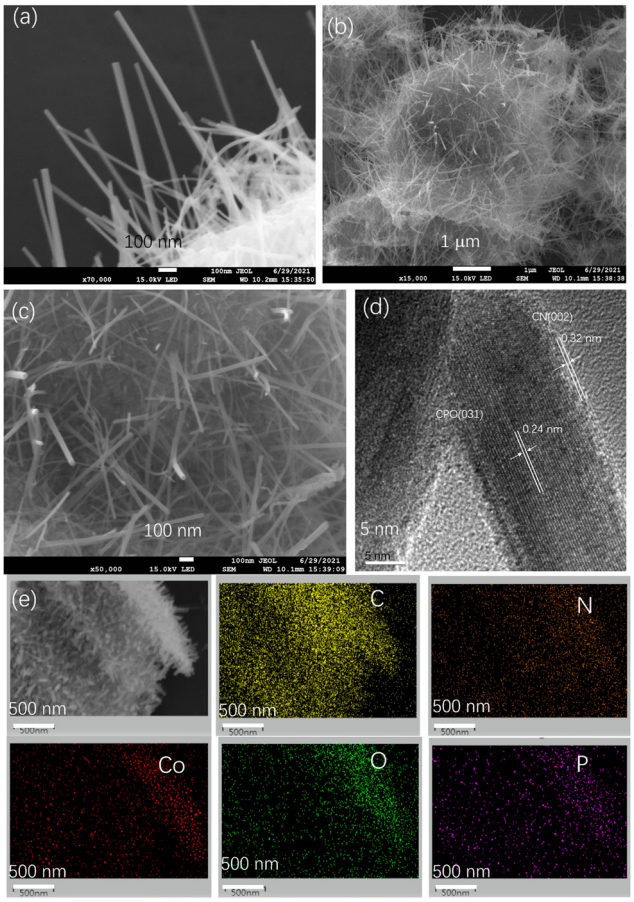

Fig. 3 SEM image of CPO (a). SEM images (b) and (c), HRTEM images (d) and element mappings (e) of 15CPO-CN.

material. The composite surface has more mesopores (1–6 nm), which are typical small mesopores. In addition, the specific surface areas of pure phase CN and 15CPO–CN are 63.1 $m^2 g^{-1}$ and 365.0 $m^2 g^{-1}$, respectively, indicating that this special composite structure can significantly increase the specific surface area (about 6 times), so that the sample has more surface active sites, which helps to improve the photocatalytic performance.

The morphology and microstructure of the samples were observed by FESEM and TEM. The SEM image in Fig. 3(a) shows that CPO appeared as nanowires with widths of 10–20 nm and lengths of several micrometers. The FESEM images of Fig. 3(b and c) show that a large number of CPO nanowires with a particle size of about 10–20 nm are embedded in the nanosheet of g-C_3N_4. From the TEM image in Fig. 3(d), it can be seen that $Co_3(PO_4)_2$ is tightly attached to the surface of g-C_3N_4, indicating that good contact is formed between CPO and CN, reducing the interfacial transfer potential energy of photogenerated electrons.[24,25] At the same time, EDS was used to further confirm the element composition in the sample, as shown in Fig. 3(e), which verified the composition of heterojunction elements in the CPO-CN composite, and successfully constructed a 1D nanowire composite structured photocatalyst (Fig. 3).

XPS was carried out to further determine the chemical composition and element state of the samples. The XPS survey spectra in Fig. 4(a) show that the C 1s peak exists at 288 eV, the N 1s peak at 398 eV, and the O 1s peak at 532 eV for CN; the Co 2p peak, O 1s and P 2p for CPO; and the small peaks of Co 2p and P 2p besides the C 1s, N 1s, and O 1s peaks for the 15CPO–CN composite, confirming that the composite photocatalyst was formed. The C 1s spectra in Fig. 4(b) show that the peak at 284.5 eV is attributed to the graphitized C atom (C–C, C═C) on the sample surface, the peak of 285.8 eV is attributed to the intermediate product of C–NH_2 bonded on the

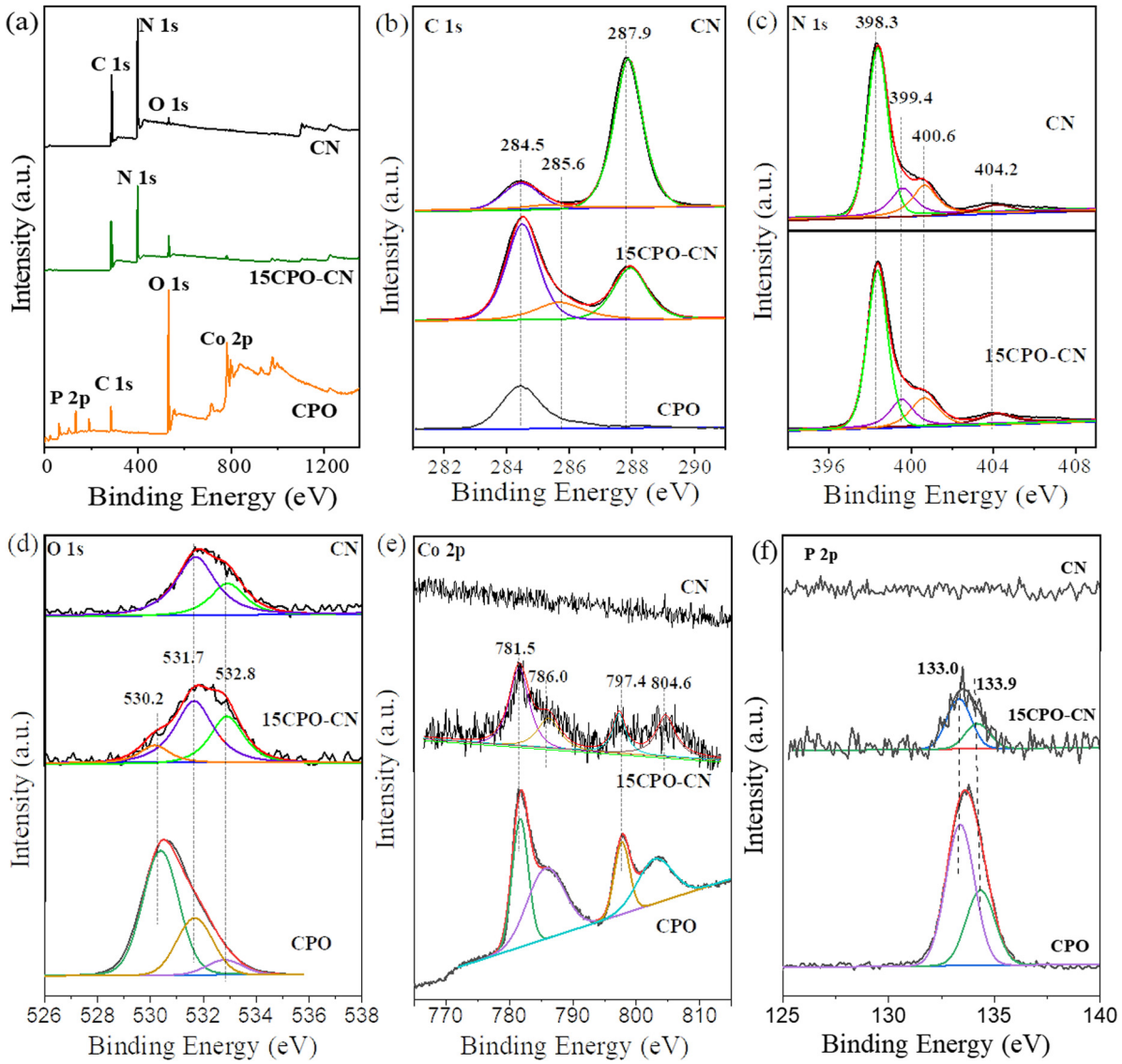

Fig. 4 XPS survey spectra (a), and high-resolution spectra of C 1s (b), N 1s (c), O 1s (d), Co 2p (e), and P 2p (f) of CN, 15CPO-CN, and CPO.

triazine ring, and the peak of 288.1 eV is attributed to the sp^2 hybrid (C–N=C) in the aromatic C–N skeleton structure.[26–28] There exists only adsorbed carbon at 284.5 eV for CPO. The intensity of the graphitized C increased drastically for 15CPO–CN. The N 1s spectra in Fig. 4(c) shows that the main peak at 398.3 eV corresponds to the sp^2 hybrid N atom in C containing a triazine ring (C–N=C), the peak at 399.4 eV is attributed to the bridged N atom in N–$(C)_3$, the peak at 400.6 eV represents the ammonia group (N–Hx), and the peak at 404 eV is attributed to the charging effect.[29,30] The O 1s spectra in Fig. 4(d) were fitted to two peaks of 531.7 eV and 532.8 eV, corresponding to the adsorbed –OH group and O_2. After the formation of the $Co_3(PO_4)_2$/g-C_3N_4 composite, a new peak of 530.2 eV appeared, which can be attributed to the O 1s signal in the phosphate group. The Co 2p spectra in Fig. 4(e) show that peaks at binding energies of 781.5 and 797.4 eV, correspond to Co $2p_{3/2}$ and Co $2p_{1/2}$ respectively, and the other two satellite peaks are located at 786.0 eV and 804.6 eV, which proves that Co exists in $Co_3(PO_4)_2$ as Co^{2+}.[31] The P 2p spectra in Fig. 4(f) exhibit peaks of P $2p_{1/2}$ and P $2p_{3/2}$ located at 132.7 eV and 133.6 eV respectively, indicating that there is a phosphorus atom in the phosphate group. Therefore, the above XPS results confirm that $Co_3(PO_4)_2$ and g-C_3N_4 exist simultaneously in the composite, which further proves that $Co_3(PO_4)_2$ and g-C_3N_4 are successfully compounded.

The light absorption property and electronic structure of the CN and CPO–CN composites were characterized using UV-vis diffuse reflection and XPS valence band spectra. The UV-vis absorption spectra in Fig. 5(a) indicate that the absorption edge of CN is about 450 nm, while CPO has a main absorption peak at about 510–550 nm. As compared with CN, the absorbance of the CPO–CN composites increases significantly within the visible light range of 500–700 nm with the increase of CPO ratio, indicating that more electrons and holes can be generated to participate in the photocatalytic reaction. According to Kubelka–Munk plots in Fig. 5(b), the band gaps of CN and CPO can be calculated as 2.70 eV and 1.93 eV respectively. The band gap for CPO is consistent with the reported value in ref. 19. The band gap for CPO–CN nanocomposites is 2.65 eV, 2.63 eV, 2.60 eV, and 2.54 eV, for 05CPO–CN, 10CPO–CN, 15CPO–CN, and 20CPO–CN, respectively.

In order to further understand the energy level arrangement of the composite photocatalyst, the VB position of the photocatalysts was detected using XPS valence band (VB) spectroscopy. Fig. 5(c) presents that the VB positions (E_{VB}) *vs.* Fermi level of CN, CPO, and 15CPO–CN are 1.89 eV, 1.39 eV, and 1.81 eV, respectively. The electrochemical energy potentials in volts of CN and CPO are estimated to be 1.65 eV and 1.15 eV (*vs.* NHE), respectively, by the formula $E_{NHE}/V = \Phi + VB - 4.44$, according to the reference standard for which 0 V *versus* NHE (reversible hydrogen electrode) equals −4.44 eV *versus* vacuum level, and the work function Φ of the analyzer is 4.20 eV. The band gap values of CN and CPO are respectively 2.70 eV and

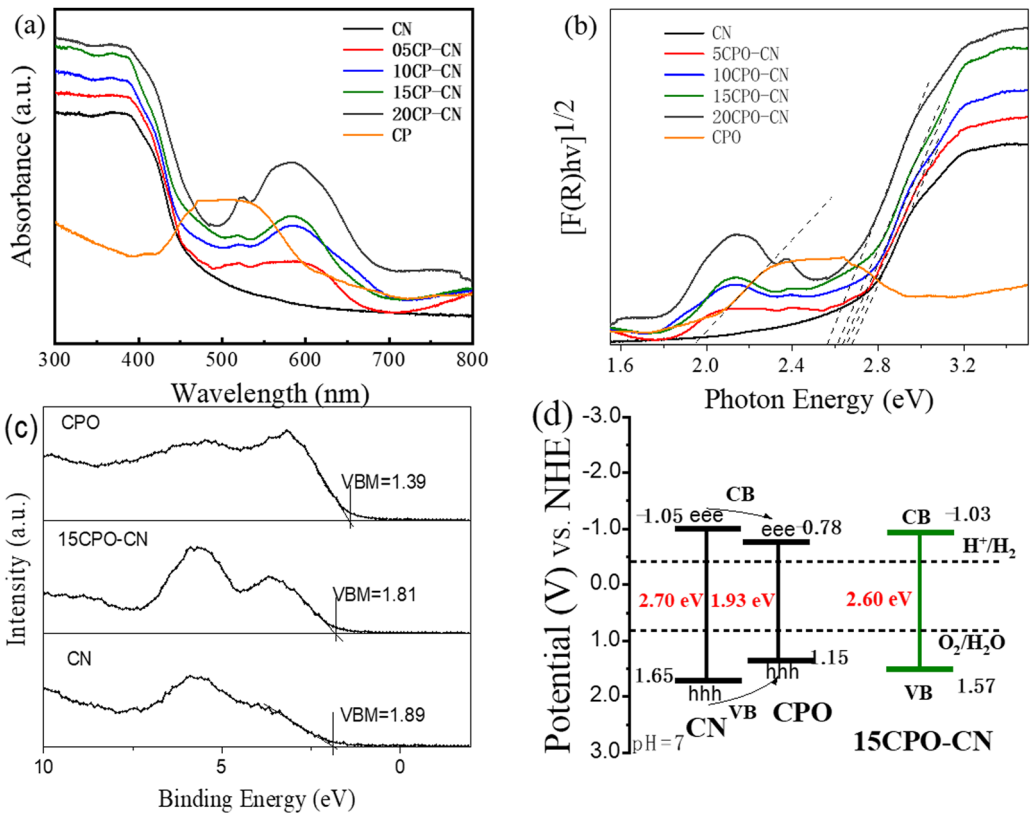

Fig. 5 UV-visible diffuse reflectance spectra (a), corresponding Kubelka–Munk plots (b), XPS valence band spectra (c), and schematic band structure of $Co_3(PO_4)_2$/g-C_3N_4 nanocomposites.

1.93 eV, obtained through the Kubelka–Munk function. The conduction band (CB) potentials are −1.05 eV and −0.78 eV for CN and CPO, respectively. The VB and CB potentials for 15CPO–CN are calculated to be 1.57 eV, and −1.03 eV in a similar manner. The energy band diagram of the catalysts is illustrated in Fig. 5(d). The CPO–CN composite constitutes a type I heterojunction, in which the photogenerated electron and hole in CN tend to be transferred to CPO nanowires, and CPO acts as a mediator of electrons.

Fig. 6(a) depicts the instantaneous photocurrent response curve (*I*–*t*) of all catalysts. After five cycles of light on–off, the electrode performance is stable under light irradiation. The photocurrent intensity of CPO–CN composites is improved by varying degrees compared with that of pure CN, and the 15CPO–CN with the strongest photocurrent intensity. Fig. 6(b) shows the photocurrent density-bias voltage curve (*J*–*V*) of the catalysts. Under continuous bias voltage, all samples can respond continuously and stably. The photocurrent density of the CPO–CN composite samples is improved to varying degrees compared with that of CN, and the photocurrent density of the 15CP–CN sample is the strongest. It demonstrates that the composites of this heterojunction structure can generate more photogenerated carriers under visible light and be effectively separated, improving the utilization of visible light, and improving the redox potential of CN,[32–36] thereby improving the visible light catalytic reaction performance of the samples. Fig. 6(c) shows the electrochemical impedance spectroscopy (EIS) of all samples. The smaller arc radius represents the lower charge transfer resistance. It is obvious that the composites exhibit a smaller arc radius, and the 15CPO–CN heterostructure has the smallest arc radius, showing excellent interfacial charge transfer performance. Fig. 6(d) shows the photoluminescence spectra (PL) of all samples, which is used to study the recombination of electron hole pairs of samples under light. All samples were excited by the same light source (wavelength: 374 nm). Pure CN showed a strong intrinsic emission band, which was attributed to direct intrinsic emission electron hole recombination. With the addition of CPO, the PL strength of CPO–CN composites decreased gradually, and 15CPO–CN with the lowest intensity. The fluorescence quenching occurs successively after the composite is formed, and the recombination rate of photogenerated carriers is lowered to improve the photocatalytic activity.[37–40] Photoelectrochemical measurements verify that the separation and migration of photogenerated carriers in the CPO–CN composites have been improved, leading to the excellent photocatalytic performance.

The hydrogen evolution performance is shown in Fig. 7(a). The hydrogen evolution rate of CPO is negligible, and CN is 2.89 μmol h^{-1}. The optimal hydrogen evolution rate of 15CPO–CN reaches 29.31 μmol h^{-1}, about 10.1 times that of CN. The hydrogen evolution rate of the mixture of CPO&CN with the same proportion is only 4.95 μmol h^{-1}. This proved that

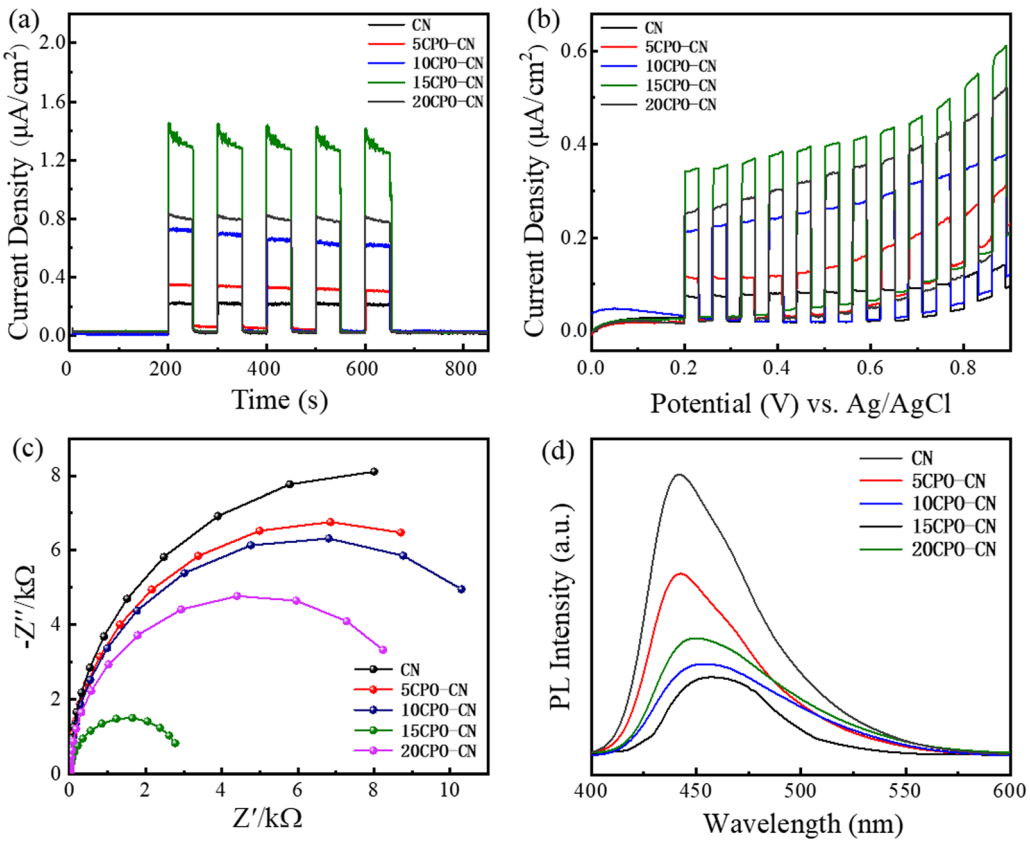

Fig. 6 Transient photocurrent response (a), photocurrent density–voltage curves (b), EIS (c), and PL (d) of CN and CPO-CN nanocomposites.

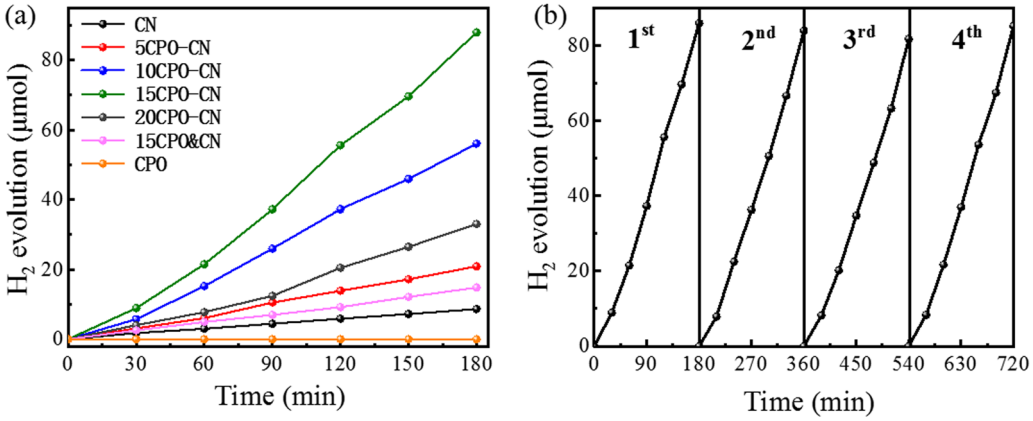

Fig. 7 Hydrogen evolution rates for the pure g-C_3N_4 and CPO/g-C_3N_4 nanocomposites (a), and the stability test of 15CPO-CN (b).

composite formation contributed to the improved hydrogen evolution rate. 15CPO–CN catalysts were tested for several cycles under the same irradiation conditions. The stability of the hydrogen evolution obtained is shown in Fig. 7(b). After four cycles of testing, the photocatalytic activity has not shown obvious changes, which proves that the photocatalytic performance of the CPO–CN composite is stable and can be reused.

The photocatalytic antibacterial activity for removing *E. coli* of CN and 15CP–CN composites was determined using a plate counting method, as shown in Fig. 8. The blank group in Fig. 8(a) is presented as a reference, and CN and 15CPO–CN photocatalysts had little effect on the concentration of Escherichia coli under dark conditions. However, upon visible light irradiation, the antibacterial removal of CN and CPO was significantly improved, as presented in Fig. 8(b and c). The concentration of *E. coli* bacteria in the 15CP–CN composite group was significantly reduced. The antibacterial rate was 95.1% higher than that in the CN group; compared with the blank group, the antibacterial rate reached 97.3%.

Fig. 9 shows the EPR spectrum of 15CPO–CN using 5,5-dimethyl-1-pyrroline *N*-oxide (DMPO) as the active capture agent to detect free radicals under visible light irradiation. In the dark state, there are no characteristic peaks of DMPO $^{\bullet}O_2^-$ (superoxide radical) and DMPO $^{\bullet}OH$ (hydroxyl radical). DMPO $^{\bullet}O_2^-$ and DMPO $^{\bullet}OH$ characteristic peaks were produced under visible light irradiation, indicating that the $^{\bullet}OH$ active group was produced by the interaction of photogenerated electrons and holes. The EPR experiment shows that hydroxyl radical ($^{\bullet}OH$) and superoxide radical $^{\bullet}O_2^-$ are the main active oxygen species (ROS) involved in photocatalysis. Reactive oxygen species (ROS) are produced by the interaction of photo-induced charge carriers with H_2O and O_2 adsorbed on the catalyst surface. Under visible light irradiation, photogenerated electrons are captured by O_2 to form $^{\bullet}O_2^-$ and react with water to form $^{\bullet}OH$. Under visible light, CN and 15CP–CN produce the photogenerated electron/hole pairs, further generating superoxide $^{\bullet}O_2^-$ and superoxyl $^{\bullet}OH$ species, ultimately inactivating the Escherichia coli, and achieving the antibacterial purpose.[43–50]

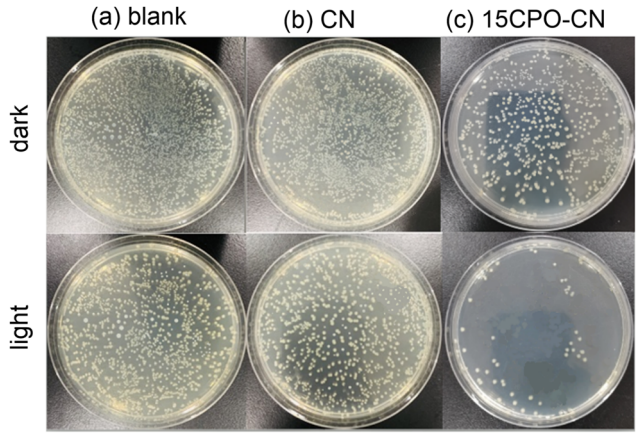

Fig. 8 The number of *E. coli* colonies under dark and visible light irradiation of CN and 15CPO–CN. Dark is the treatment without light irradiation, and the blank is the reference.

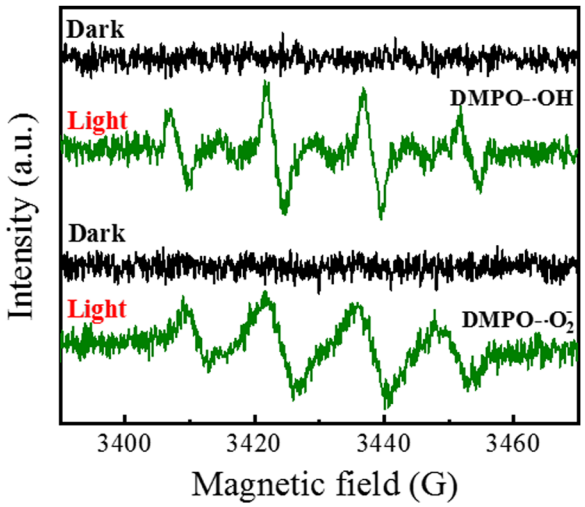

Fig. 9 EPR spectra of 15CPO–CN in a methanol dispersion for superoxide ($^{\bullet}O_2^-$) and an aqueous solution for hydroxyl radical ($^{\bullet}OH$) under visible light irradiation.

Taking the above characterization results into consideration, the photocatalytic mechanism of CPO–CN composites was proposed. CPO–CN composites constituted a type I heterojunction. The electrons in the VB of CPO and CN were excited to the CB, leaving holes in the VB. The CB electrons of CN transferred quickly to the CB of CPO to generate H_2 from H^+ in water.[50] The synergistic effect between $Co_3(PO_4)_2$ and g-C_3N_4 boosted the light harvesting in an extended visible light range, and effectively inhibited the recombination of photogenerated electron/hole pairs. In addition, the 1D nanowire heterostructure increased the interfacial contact area to realize rapid interfacial charge separation. On the other hand, 15CPO–CN generates photogenerated electron/hole pairs, which in turn generates a superoxide radical ($^{\bullet}O_2^-$) and hydroxyl radical ($^{\bullet}OH$). These free radicals destroy the cell membrane of *E. coli* through photocatalytic oxidation, inactivating *E. coli* to achieve the antibacterial purpose.

4. Conclusions

In summary, we have successfully prepared $Co_3(PO_4)_2$/g-C_3N_4 nanowire composites by calcining melamine and $Co_3(PO_4)_2$ nanowires, in which a certain amount of $Co_3(PO_4)_2$ nanowires is embedded on the matrix of g-C_3N_4 sheets. The optimal photocatalytic hydrogen rate of 15CPO–CN reached 29.31 μmol h^{-1}, much higher than that of CN (2.89 μmol h^{-1}) and CPO, and it showed enhanced antibacterial activity for removing *E. coli* as well. The configuration of the 1D/2D hybrid heterojunction increased the specific surface area to provide more reactive sites, extended the visible light absorption range, and promoted interfacial charge transfer and separation. This work provides a prospective way to design a composite photocatalyst with enhanced photocatalytic hydrogen production and photocatalytic oxidation of bacteria.

Author contributions

The manuscript was written through contributions of all authors. All authors have given approval to the final version of the manuscript.

Conflicts of interest

The authors declare no conflict of interest.

Acknowledgements

This work was supported by the National Natural Science Foundation of China (52271250).

References

1 A. Houas, H. Lachheb, M. Ksibi, E. Elaloui, C. Guillard and J.-M. Herrmann, Photocatalytic degradation pathway of methylene blue in water, *Appl. Catal., B*, 2001, **31**, 145–157.
2 J. L. Li, M. Zhang, Z. J. Guan, Q. Y. Li, C. Q. He and J. J. Yang, Synergistic effect of surface and bulk single-electron-trapped oxygen vacancy of TiO_2 in the photocatalytic reduction of CO_2, *Appl. Catal., B*, 2017, **206**, 300–307.
3 S. B. Jaffri and K. S. Ahmad, Augmented photocatalytic, antibacterial and antifungal activity of prunosynthetic silver nanoparticles, *Artif. Cells, Nanomed., Biotechnol.*, 2018, **46**, 127–137.
4 B. Liu, C. H. Wu, J. W. Miao and P. D. Yang, All inorganic semiconductor nanowire mesh for direct solar water splitting, *ACS Nano*, 2014, **8**, 11739–11744.
5 Y. Liao, J. Yang, G. Wang, J. Wang, K. Wang and S. Yan, Hierarchical porous NiO as a noble-metal-free cocatalyst for enhanced photocatalytic H_2 production of nitrogen-deficient g-C_3N_4, *Rare Met.*, 2022, **41**, 396–405.
6 Y. Z. Liu, X. J. Li, H. He, S. G. Yang, G. H. Jia and S. M. Liu, CoP imbedded g-C_3N_4 heterojunctions for highly efficient photo, electro and photoelectrochemical water splitting, *J. Colloid Interface Sci.*, 2021, **599**, 23–33.
7 Y. Zhou, L. Zhang, J. Liu, X. Fan, B. Wang and M. Wang, Brand new P-doped g-C_3N_4: enhanced photocatalytic activity for H_2 evolution and rhodamine B degradation under visible light, *J. Mater. Chem. A*, 2015, **3**(7), 3862–3867.
8 X. J. Wang, X. Tian, Y. J. Sun, J. Y. Zhu, H. Y. Mu, F. T. Li and J. Zhao, Enhanced Schottky effect of a 2D–2D CoP/g-C_3N_4 interface for boosting photocatalytic H_2 evolution, *Nanoscale*, 2018, **10**, 12315–12321.
9 H. Zhang, L. Li, Q. Li, T. Ma, J. Gao and S. Gao, Graphitic carbon nitride loaded with bismuth nanoparticles displays antibacterial photocatalytic activity, *Rare Met.*, 2022, **41**, 1570–1582.
10 H. Xu, R. Xiao, J. Huang, Y. Jiang, C. Zhao and X. Yang, In situ construction of protonated g-C_3N_4/Ti_3C_2 MXene Schottky heterojunction for efficient photocatalytic hydrogen production, *Chin. J. Catal.*, 2021, **42**, 107–114.
11 W. N. Xing, W. G. Tu, Z. G. Han, Y. D. Hu, Q. Q. Meng and G. Chen, Template-induced high-crystalline g-C_3N_4 nanosheets for enhanced photocatalytic H_2 evolution, *ACS Energy Lett.*, 2018, **3**, 514–519.
12 X. Liu, C. Zhao, T. Muhmood and X. Yang, Regulating the assembly of precursors of carbon nitrides to improve photocatalytic hydrogen production, *Catalysts*, 2022, **12**, 1634.
13 H. X. Liu, X. J. Liu, Z. Y. Mao, Z. Zhao, X. Y. Peng, J. Luo and X. M. Sun, Plasma-activated $Co_3(PO_4)_2$ nanosheet arrays with Co^{3+}-Rich surfaces for overall water splitting, *J. Power Sources*, 2018, **400**, 190–197.
14 Z. Geng, M. Yang, X. Qi, Z. Y. Li, X. Yang, M. X. Huo and J. C. Crittenden, $Co_3(PO_4)_2$/Ag_3PO_4 with enhanced simulated sunlight photocatalytic activity toward ofloxacin degradation and mechanism insight, *J. Chem. Technol. Biotechnol.*, 2019, **94**, 1660–1669.
15 W. L. Shi, M. Y. Li, X. L. Huang, H. J. Ren, C. Yan and F. Guo, Facile synthesis of 2D/2D $Co_3(PO_4)_2$/g-C_3N_4 heterojunction for highly photocatalytic overall water splitting under visible light, *Chem. Eng. J.*, 2020, **382**, 122960.

16 W. Shi, M. Li, X. Huang, H. Ren, F. Guo and C. Yan, Three-dimensional Z-Scheme $Ag_3PO_4/Co_3(PO_4)_2$@Ag heterojunction for improved visible-light photocatalytic degradation activity of tetracycline, *J. Alloys Compd.*, 2019, **81**, 152883.

17 A. Samal, S. Swain, B. Satpati, D. P. Das and B. K. Mishra, 3D $Co_3(PO_4)_2$–Reduced Graphene Oxide Flowers for Photocatalytic Water Splitting: A Type II Staggered Heterojunction System, *ChemSusChem*, 2016, **9**, 3150–3160.

18 W. L. Shi, C. Liu, M. Y. Li, X. Lin, F. Guo and J. Y. Shi, Fabrication of ternary $Ag_3PO_4/Co_3(PO_4)_2$/g-C_3N_4 heterostructure with following Type II and Z-Scheme dual pathways for enhanced visible-light hotocatalytic activity, *J. Hazard. Mater.*, 2020, **389**, 121907.

19 M. Zhu, M. Han, C. Zhu, L. Hu, H. Huang, Y. Liu and Z. Kang, Strong coupling effect at the interface of cobalt phosphate-carbon dots boost photocatalytic water splitting, *J. Colloid Interface Sci.*, 2018, **530**, 256–263.

20 R. Tong, X. Wang, X. Zhou, Q. Liu, H. Wang, X. Peng, X. Liu, Z. Zhang, H. Wang and P. D. Lund, Cobalt-phosphate modified $TiO_2/BiVO_4$ nanoarrays photoanode for efficient water splitting, *Int. J. Hydrogen Energy*, 2017, **42**, 5496–5504.

21 Y. G. Tan, Z. Shu, J. Zhou, X. L. Wang, T. T. Li, W. B. Wang and Z. L. Zhao, Facile preparation of hollow-nanosphere based mesoporous g-C_3N_4 for highly enhanced visible-light-driven photocatalytic hydrogen evolution, *Appl. Surf. Sci.*, 2018, **455**, 591–598.

22 J. Safaei, H. Ullah, N. A. Mohamed, M. F. M. Noh, M. F. Soh, A. A. Tahir, N. A. Ludin, M. A. Ibrahim, W. N. R. W. Isahak and M. A. M. Teridi, Enhanced photoelectrochemical performance of Z-scheme g-$C_3N_4/BiVO_4$ photocatalyst, *Appl. Catal., B*, 2018, **234**, 296–310.

23 J. P. Zou, L. C. Wang, J. M. Luo, Y. C. N. Q. J. Xing, X. B. Luo, H. M. Du, S. L. Luo and S. L. Suib, Synthesis and efficient visible light photocatalytic H_2 evolution of a metal-free g-C_3N_4/graphene quantum dots hybrid photocatalyst, *Appl. Catal., B*, 2016, **193**, 103–109.

24 W. K. Jo and N. C. S. Selvam, Z-scheme CdS/g-C_3N_4 composites with RGO as an electron mediator for efficient photocatalytic H_2 production and pollutant degradation, *Chem. Eng. J.*, 2017, **317**, 913–924.

25 V. G. Deonikar, K. K. Reddy, W. J. Chung and H. Kim, Facile synthesis of Ag_3PO_4/g-C_3N_4 composites in various solvent systems with tuned morphologies and their efficient photocatalytic activity for multi-dye degradation, *J. Photochem. Photobiol., A*, 2019, **368**, 168–181.

26 D. Long, W. L. Chen, S. H. Zheng, X. Rao and Y. P. Zhang, Barium- and Phosphorus-Codoped g-C_3N_4 Microtubes with Efficient Photocatalytic H_2 Evolution under Visible Light Irradiation, *Ind. Eng. Chem. Res.*, 2020, **59**, 4549–4556.

27 T. T. Xiao, Z. Tang, Y. Yang, L. Q. Tang, Y. Zhou and Z. G. Zou, In situ construction of hierarchical WO_3/g-C_3N_4 composite hollow microspheres as a Z-scheme photocatalyst for the degradation of antibiotics, *Appl. Catal., B*, 2018, **220**, 417–428.

28 M. Z. You, J. Q. Pan, C. Y. Chi, B. B. Wang, W. J. Zhao, C. S. Song, Y. Y. Zheng and C. R. Li, The visible light hydrogen production of the Z-Scheme Ag_3PO_4/Ag/g-C_3N_4 nanosheets composites, *J. Mater. Sci.*, 2018, **53**, 1978–1986.

29 R. C. Shen, W. Liu, D. D. Ren, J. Xie and X. Li, $Co_{1.4}Ni_{0.6}P$ cocatalysts modified metallic carbon black/g-C_3N_4 nanosheet Schottky heterojunctions for active and durable photocatalytic H_2 production, *Appl. Surf. Sci.*, 2019, **466**, 393.

30 F. Guo, W. Shi, M. Li, Y. Shi and H. Wen, 2D/2D Z-scheme heterojunction of $CuInS_2$/g-C_3N_4 for enhanced visible-light-driven photocatalytic activity towards the degradation of tetracycline, *Sep. Purif. Technol.*, 2019, **210**, 608–615.

31 D. Long, W. Chen, X. Rao, S. H. Zheng and Y. P. Zhang, Synergetic effect of C_{60}/g-C_3N_4 nanowire composite for enhanced photocatalytic H_2 evolution under visible light irradiation, *ChemCatChem*, 2020, **12**, 2022–2031.

32 S. Patnaik, D. P. Sahoo and K. Parida, An overview on Ag modified g-C_3N_4 based nanostructured materials for energy and environmental applications, *Renewable Sustainable Energy Rev.*, 2018, **82**, 1297–1312.

33 F. He, Z. X. Wang, Y. X. Li, S. Q. Peng and B. Liu, The nonmetal modulation of composition and morphology of g-C_3N_4-based photocatalysts, *Appl. Catal., B*, 2020, **269**, 118828.

34 S. S. Li, Y. N. Peng, C. Hu and Z. H. Chen, Self-assembled synthesis of benzene-ring-grafted g-C_3N_4 nanotubes for enhanced photocatalytic H_2 evolution, *Appl. Catal., B*, 2020, **279**, 119401.

35 J. Duan, S. Chen, M. Jaroniec and S. Z. Qiao, Porous C_3N_4 nanolayers@N-graphene films as catalyst electrodes for highly efficient hydrogen evolution, *ACS Nano*, 2015, **9**(1), 931–940.

36 Y. J. Ren, D. Q. Zeng and W. J. Ong, Interfacial engineering of graphitic carbon nitride (g-C_3N_4)-based metal sulfide heterojunction photocatalysts for energy conversion: A review, *Chin. J. Catal.*, 2019, **40**, 289–319.

37 Z. Li, Y. N. Ma, X. Y. Hu, E. Z. Liu and J. Fan, Enhanced photocatalytic H_2 production over dual-cocatalyst-modified g-C_3N_4 heterojunctions, *Chin. J. Catal.*, 2019, **40**, 434–445.

38 H. L. Dou, D. Long, S. H. Zheng and Y. P. Zhang, A facile approach to synthesize graphitic carbon nitride microwires for enhanced photocatalytic H_2 evolution from water splitting under full solar spectrum, *Catal. Sci. Technol.*, 2018, **8**, 3599–3609.

39 P. Wang, S. H. Sun, X. Y. Zhang, X. Ge and W. Lu, Efficient degradation of organic pollutants and hydrogen evolution by g-C_3N_4 using melamine as the precursor and urea as the modifier, *RSC Adv.*, 2016, **6**, 33589–33598.

40 D. Long, Z. Q. Chen, X. Rao and Y. P. Zhang, Sulfur-doped g-C_3N_4 and $BiPO_4$ nanorod hybrid architectures for enhanced photocatalytic hydrogen evolution under visible light irradiation, *ACS Appl. Energy Mater.*, 2020, **3**, 5024–5030.

41 W. Zhang, J. Zhang and F. Dong, Facile synthesis of *in situ* phosphorus-doped g-C_3N_4 with enhanced visible light photocatalytic property for NO purification, *RSC Adv.*, 2016, **6**, 88085–88089.

42 G. Liu, P. Niu, C. H. Sun, S. C. Smith, Z. G. Chen, G. Q. Lu and H. M. Cheng, Unique electronic structure induced high

photoreactivity of sulfur-doped graphitic C_3N_4, *J. Am. Chem. Soc.*, 2010, **132**, 11642–11648.

43 M. K. Bhunia, K. Yamauchi and K. Takanabe, Harvesting solar light with crystalline carbon nitrides for efficient photocatalytic hydrogen evolution, *Angew. Chem., Int. Ed.*, 2014, **53**, 11001–11005.

44 F. Wang, Y. Feng, P. Chen, Y. Wang, Y. Su, Q. Zhang and G. Liu, Photocatalytic degradation of fluoroquinolone antibiotics using ordered mesoporous g-C_3N_4 under simulated sunlight irradiation: Kinetics, mechanism, and antibacterial activity elimination, *Appl. Catal., B*, 2018, **227**, 114–122.

45 L. Sun, T. Du, C. Hu, J. Chen, J. Lu, Z. Lu and H. Han, Antibacterial activity of graphene Oxide/g-C_3N_4 composite through photocatalytic disinfection under visible light, *ACS Sustainable Chem. Eng.*, 2017, **10**, 8693–8701.

46 L. W. Wang, X. Zhang, X. Yu, F. E. Gao, Z. Y. Shen, X. L. Zhang and C. Chen, An All-Organic Semiconductor C_3N_4/PDINH Heterostructure with Advanced Antibacterial Photocatalytic Therapy Activity, *Adv. Mater.*, 2019, **6**, 1901965.

47 Q. Xiang, J. Yu and M. Jaroniec, Preparation and enhanced visible-light photocatalytic H_2-production activity of graphene/C_3N_4 composites, *J. Phys. Chem. C*, 2011, **15**, 7355–7363.

48 J. L. Li, X. Bai, X. Rao and Y. P. Zhang, Heterojunction of WO_3 particle and g-C_3N_4 nanowire for enhanced photocatalytic hydrogen evolution, *ChemistrySelect*, 2021, **6**, 8182–8187.

49 D. Yan, X. Wu, J. Y. Pei, C. C. Wu, X. M. Wang and H. Y. Zhao, Construction of g-C_3N_4/TiO_2/Ag composites with enhanced visible-light photocatalytic activity and antibacterial properties, *Ceram. Int.*, 2020, **46**, 696–702.

50 W. W. Liu, J. Pan and R. F. Peng, Shape-dependent hydrogen generation performance of PtPd bimetallic co-catalyst coupled with C_3N_4 photocatalyst, *Rare Met.*, 2021, **40**, 3554–3560.